Event-Driven Hyporheic Exchange during Single and Seasonal Rainfall in a Gaining Stream

Chengpeng Lu [1] · Keyan Ji [1] · Yong Zhang [2] · Jan H. Fleckenstein [3] ·
Chunmiao Zheng [4] · Kate Salsky [2]

Abstract

This study combined a reach-scale field survey and numerical modelling analysis to reveal the pattern of transient hyporheic exchange driven by rainfall events in the Zhongtian River, Southeast China. Field observations revealed hydrodynamic properties and flux variations in surface water (SW)/ groundwater (GW), suggesting that the regional groundwater recharged the study reach. A two-step numerical modelling procedure, including a hydraulic surface flow model and a groundwater flow model, was then used to interpret the transient hyporheic flow system. The hyporheic exchange exhibited strong temporal evolution in the study reach, as indicated by the rainfall event-driven hyporheic exchange. The reversal of the hydraulic gradient and transient hyporheic exchange were simulated using numerical simulation. Anisotropic hydraulic conductivity is the key to generating transient hyporheic exchange. A revised conceptual model was used to interpret the observed temporal patterns in hyporheic exchange. The seasonal rainfall events generate transient hyporheic exchange, and the pattern of transient hyporheic exchange indicates that transient hyporheic exchange appears only after an increased phase of the river stage but does not last long. The temporal pattern of hyporheic exchange can significantly affect the hydrodynamic exchange and the evolution of hydrology in the hyporheic zone for a gaining stream, and these results have important guiding significance for the comprehensive management of surface water and groundwater quantity and quality.

✉ Chengpeng Lu
   luchengpeng@hhu.edu.cn

✉ Yong Zhang
   yzhang264@ua.edu

Extended author information available on the last page of the article

1 Introduction

Hyporheic exchange (HE), referring to the water from a stream that enters the hyporheic zone (HZ) and then returns to the stream, is driven by hydraulic gradients at the streambed surface, which evolve from the interplay between streambed pressure distributions caused by the interactions among surface water (SW) hydraulics, streambed morphology, and ambient groundwater (GW) heads (Cardenas and Wilson 2007; Trauth et al. 2013). Here, HE is broadly defined as any kind of flow in the HZ affected by the dynamic interplay between SW and GW (Han and Endreny 2014). Moreover, hyporheic flow dynamics and flow paths may be affected by stage variations (Gerecht et al. 2011), wood addition in the channel (Sawyer and Cardenas 2012), and hydraulic jumps (Endreny et al. 2011a, b; Trauth et al. 2013). There has been a recent focus on understanding spatial variability in HE across different morphological units, mainly under steady baseflow conditions (Buffington and Tonina 2009; Hester and Doyle 2008). Understanding the complexity of hyporheic processes at a fine scale is important for the management of changing river systems (Casas-Mulet et al. 2015).

Rainfall can affect the transient dynamics of hyporheic flow since it can alter HZ hydrodynamics in a way similar to the regulation of a reservoir or other transients in stream discharge (Casas-Mulet et al. 2015; Siergieiev et al. 2015) by causing reversals of the hydraulic gradient between GW and SW and changes in the pressure distribution at the streambed surface. GW dynamics are also affected by rainfall events, which account for the difference between rainfall and other transients in stream discharge. Studies have shown that the ambient hydraulic gradient between GW and SW can be reversed due to rainfall (Weber et al. 2013; Zhou et al. 2018). For example, Dudley-Southern and Binley (2015) found that storm events led to a temporary reversal of the vertical hydraulic gradient up to 30 cm beneath the riverbed. The reversal of the hydraulic gradient was also driven by seasonal hydrological events, as has been reported by other studies (e.g., Storey et al. 2003). Storey et al. (2003) concluded that the hydraulic conductivity of the HZ, the hydraulic gradient, and the flux of GW can each change in a season, causing a reversal of flow paths in the alluvium and a reduction in exchange flows from summer to the following fall and spring. The physical mechanism of flow path reversal and exchange flow transition, however, were not revealed by Storey et al. (2003). However, the SW was taken as a constant head boundary, and the spatiotemporal hydraulic head in the stream was not considered in their model. Our study filled these knowledge gaps.

Moreover, it is difficult to measure HEF directly in the field which leads to the lack of comparison between the observations and calculations. However, the error caused by the asynchrony and spatial discretization of flow measurement in the field work will not appear in the numerical simulation. When combined with a hydrological model, numerical simulation can better reflect the dynamic changes in HEF. To further understand the spatiotemporal variation in HE related to storm events and seasonal hydrological events at the reach scale, it is necessary to combine field investigation with numerical simulation, motivating this study.

This study aims to explore the temporal evolution of HEF dynamics in natural rivers by systematically combining a detailed field survey and hyporheic modelling, as this research has rarely been done before. The transient hyporheic system of HEF for the Zhongtian River during rainfall events will be evaluated and numerically simulated.

2 Materials and Method

2.1 Study Site

The Zhongtian River is a second-order stream in Jiangsu Province, Southeast China (Fig. 1). It flows from south to north and eventually drains to Lake Tianmu, with a drainage area of ~47.43 km². The basin contains mainly low hills, and the elevation is between 17.8 m and 531.5 m. The climate of the study site is subtropical monsoon, and the temperature and humidity significantly differ between seasons. The annual average temperature is 17.5 °C, and the annual rainfall is 1149.7 mm. The headwaters of this reach are in the Tianmu Lake Water Preserve, and the drainage area is mostly forested with some open space, limited residential development, and small-scale agriculture. The selected river reach (Fig. 1) is approximately 30 m long and 10 m wide. Three instream sandbars exist in the reach. Moreover, hardy shrubs keep the sandbars stable during flood processes.
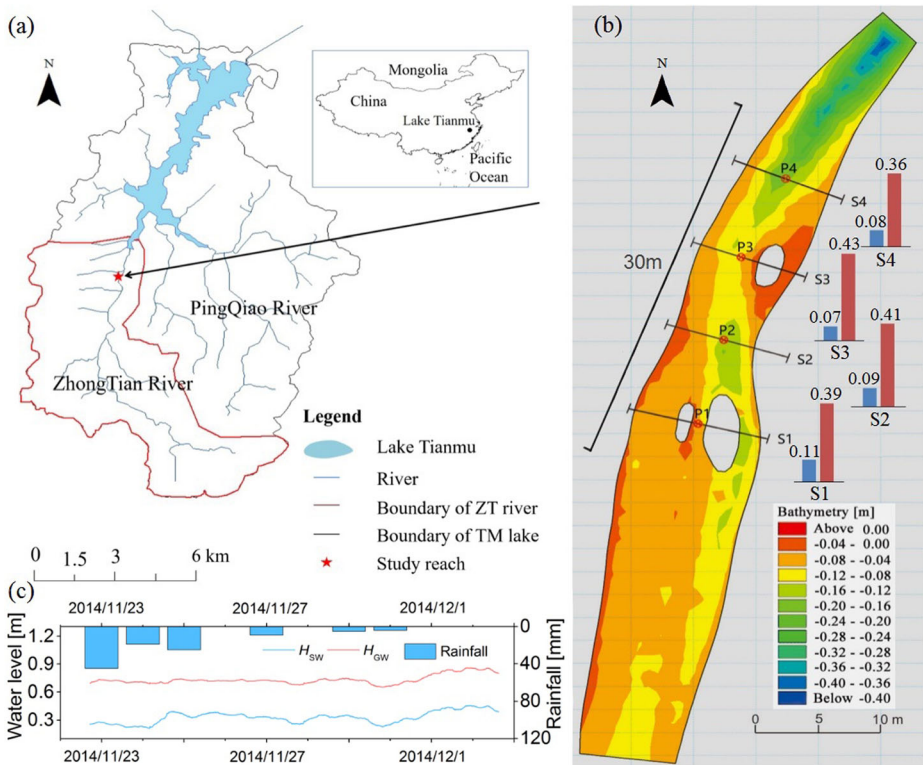
Fig. 1 Map of the Zhongtian River and Lake Tianmu (a). The cross-sections for flow measurement and the local topographical features (b). The measured time series data: relative water level of the SW (H_{SW}) and GW (H_{GW}) and the rainfall during the investigated period in (c). The three grey areas in the channel seen in the right figure represent instream sandbars. The topography was measured on Nov. 22, 2014. Measured flow discharges at four cross-sections from S1 to S4 on Nov. 22, 2014 (blue bar) and Dec. 2, 2014 (red bar) are shown in the form of a bar chart beside each section in (b), and the unit is m³/s

2.2 Field Work

We collected sand columns from 12 cores and then analysed grain size in the laboratory. The grain size was measured using 7 sieves (0.075 to 2 mm) for the coarser media and lasing sieving (LS13320, Beckman Coulter) for the finer media. The streambed is mainly composed of poorly graded gravels and sands with underlying silt and humus clay lenses. During the field survey, the hydraulic conductivity (K) of the streambed was estimated using the in-situ falling head permeameter method.

The hydrodynamic and thermal conditions in the river, GW, and HZ were continuously recorded and analysed for ten days from 11/23/2014 to 12/02/2014. The GW observation well was located ~67 m from the river channel. Two flow measurements at four sections (S1 to S4 shown as Fig. 1) were conducted on Nov. 22, 2014 and Dec. 2, 2014.

2.3 Modelling the Two-Dimensional Stream Flow

We modelled the 2D hydrodynamics of the Zhongtian River using the commercial MIKE 21 Flow Model (DHI, Inc.). Notably, a detailed, coupled SW-GW flow model could not be reliably built due to the lack of a detailed hydrogeological description for this site.

The MIKE 21 flexible mesh module (FM) was used to model the 2D distribution of flow velocity, water depth, and surface elevation. Based on the numerical solution of the nonlinear formulation of the 2D shallow water flow equations, the model considered certain factors important for the calculation of the current speed. According to the measured topography and elevation data of the study area, the channel features were analysed. The sand columns from 12 cores were collected to estimate the hydraulic conductivity (K) of the streambed, and the bed resistance was analysed. The measured data of water temperature, water level and velocity were collected upstream and downstream and at monitoring points in each section and were taken as boundary conditions. Considering the very low gradient and flow velocity noted from in-situ observations, we selected a sufficiently fine time step (300 s).

We modelled the hydrodynamic process from 11/22/2018 to 12/02/2018. A temporal survey of velocity and water depth was used to calibrate and enhance the confidence of the numerical modelling. A field elevation survey and auto-recorded pressure measurements at the upstream and downstream boundaries were also incorporated into the model. Manning's roughness coefficient n (=15.5 m$^{1/3}$/s) was obtained based on the principle of optimizing the simulation effect of the river velocity field, and the difference between the calculated flow velocity and the measured value was made as small as possible by adjusting the Manning roughness coefficient within the empirical range of the roughness coefficient.

2.4 Three-Dimensional Groundwater Flow Model

The coupled modelling framework in this study site was as follows: the water surface elevation of the study channel, obtained from the MIKE 21 model, was set as an upper Dirichlet boundary condition for the GW flow model. The modelled transient pressure can drive a complex HE. The GW flow model was built using MODFLOW (Harbaugh 2005). A time step of 3 h was selected in the GW simulation to capture the relatively slow velocity. We built a 10-layer numerical model to simulate the hyporheic flow. The areal extent (shown in Fig. 1) and the stress period of the GW model were both the same as those in the stream flow model. The total thickness of the 3D GW model was 1 m, which was uniformly divided into ten 10-cm-

thick layers, and the horizontal resolution was 40 cm × 40 cm in length and width (with 69 columns and 165 rows). The bottom boundary of the GW model was a general head boundary (GHB), which was chosen to efficiently simulate the upward GW flux. All the lateral boundaries were set to no-flow boundary conditions since field investigations implied negligible lateral inflow/outflow at the study reach compared with the vertical GW flux. The pattern of groundwater fluxes was compared with the general variation pattern of the flow measurements, to attain the numerical simulation in this study.

2.5 Seasonal Hydrologic Variation Model

It is necessary to check the hypothesis that seasonal variations in hydrologic conditions can generate the same response as those generated by strictly event-scale drivers. To investigate the change in hydraulic head in the HZ under the condition of seasonal hydrologic variation, a new coupled numerical model was developed to simulate the HE behaviour lasting for a hydrologic year. The average daily river stage for one year was considered as the input of the MODFLOW, and the coupled model generated the hydraulic head field of the HZ. The measured river stage of 2012 was selected based on a long time series frequency analysis. Specifically, to quantify the effect of time scale on the transient HE, the time step was set as 4.6 days which is much larger than that of the previous model.

3 Results

3.1 Hydrological and Thermal Investigations in the Field

Seven sand cores exhibited relatively low levels of K varying from 0.02 m/d to 0.77 m/d, while the K values for the other two samples were as high as 1.38 m/d and 12.25 m/d, respectively, implying a strong spatial variation in K. Three rainfall events of 89 mm, 9 mm, and 9 mm were observed on Nov. 23–25, Nov. 27, and Nov. 29–30 (Fig. 1c). The stream stage had a 1 ~ 2 day delay after rainfall events. Although the total rainfall was small and had a short duration, the steeply sloped catchment caused a sizable increase in the stream stage. Comparably, the GW level showed hysteretic fluctuations with the increase in water level being relatively small compared to the stream stage. The difference between the increment of the GW table and stream stage indicated the variation in the regional hydraulic gradient from GW to SW. Although the variation in GW levels was only slightly smaller than that of the river stage, the GW level remained apparently higher than that of the river stage (Fig. 1c). Hence, the overall gaining condition of the stream did not change during the entire observation period.

Two measurements of river discharges were performed at four sections from S1 to S4 (Fig. 1b). The average streamflow increased by approximately 4.6 times from 0.088 m³/s to 0.398 m³/s. However, the discharges did not strictly decrease from S1 to S4 in either measurement, indicating that both gaining and losing conditions were recorded in the three stream segments. In comparison with the two flow measurements, the rainfall events not only pushed the stream flow increase substantially but also overturned the HF between the three river segments. The HF at the two stream segments of S1-S2 and S2-S3 change from downward to upwelling flow, and the third segment of S3-S4 changed from upwelling to downward flow. It can be inferred that the local upwelling and downward hyporheic flow of the river were reversed by rainfall events. Since the GW table was consistently greater than the

stream stage (Fig. 1c), this reversal of local upwelling or downward flux conditions was the result of transient HE driven by rainfall events. Rainfall events have important effects on both the HEF and the HF directions.

3.2 Simulation of Transient Hyporheic Flow

Field observations were used to calibrate the model. For example, for the 2D stream flow dynamics model, we calibrated the model using the spatial distribution of water depth and the mean velocity. At the beginning of our field observation, the water depth and the flow velocity were measured at 25 locations in the channel. The model results generally matched (unbiased) these measurements (Fig. 2), although an exact fit between the model and measurements could not be made due to the inevitable simplification of the medium properties in the model.

Based on the field investigation, riverbed sediments were mostly composed of gravel and clay. Due to the lack of finer geophysical investigations, a homogenous and anisotropic hydraulic conductivity was initially used for the hyporheic flow model. Through several groups of simulations with different Kz/Kx ratios, the influence of different anisotropy ratios on the simulation results was obtained, and the anisotropy ratio of Kz/Kx was set at 10^{-4}. The spatiotemporal HEFs were obtained for the shallowest layer of the numerical model. The numerical modelling results of the integrated SW and GW flow model are shown in Figs. 3 and 4. The simulated hyporheic flux is shown in Fig. 3. The red line in Fig. 3 delineates the boundary between the upward and downward flux zones simulated with our numerical model, and this boundary line is located around S1 at the beginning. The transient hyporheic flow was successfully modelled from day 1 to day 4. For example, the area above the red line in the first plot shown in Fig. 3a experienced temporal HE on 3 days during rainfall. The significant downward fluxes were then identified by the model, as shown by the graphs on days 2 and 3 during the 89-mm rainfall event occurring on 11/23/2014 ~ 11/25/2014 (Fig. 3b~c). After that, no reverse of the flux direction was observed, likely due to the small rainfall in the subsequent events (i.e., two 9-mm rainfall events on 11/27 and 11/29 to 11/30, respectively, which might be too small to trigger temporal HE) (Fig. 3f~j).

One representative observation point was selected for each of the four cross sections (P1, P2, P3, and P4) to analyse the vertical variation in the hydraulic head and the evolution of HE (Fig. 4). Figure 4a~d show the simulated hydraulic head for each layer and the resultant
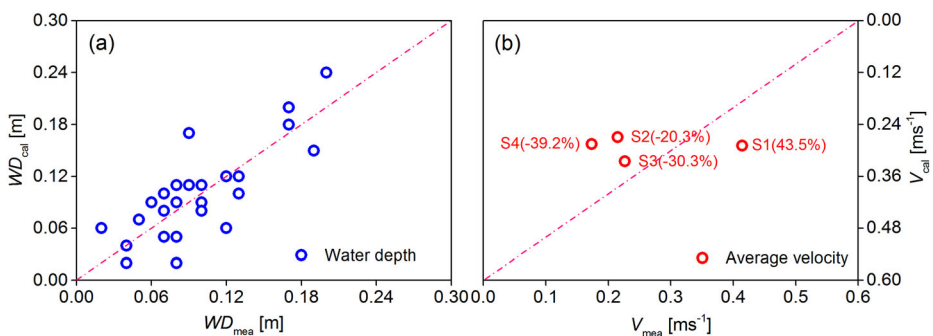

Fig. 2 The measured water depth and stream velocity versus the numerical model calculations shown in (a) and (b) respectively. At the beginning of observation, the water depth and average stream velocity were measured at 25 locations along the 4 sections using the measuring pod and flow metre, respectively
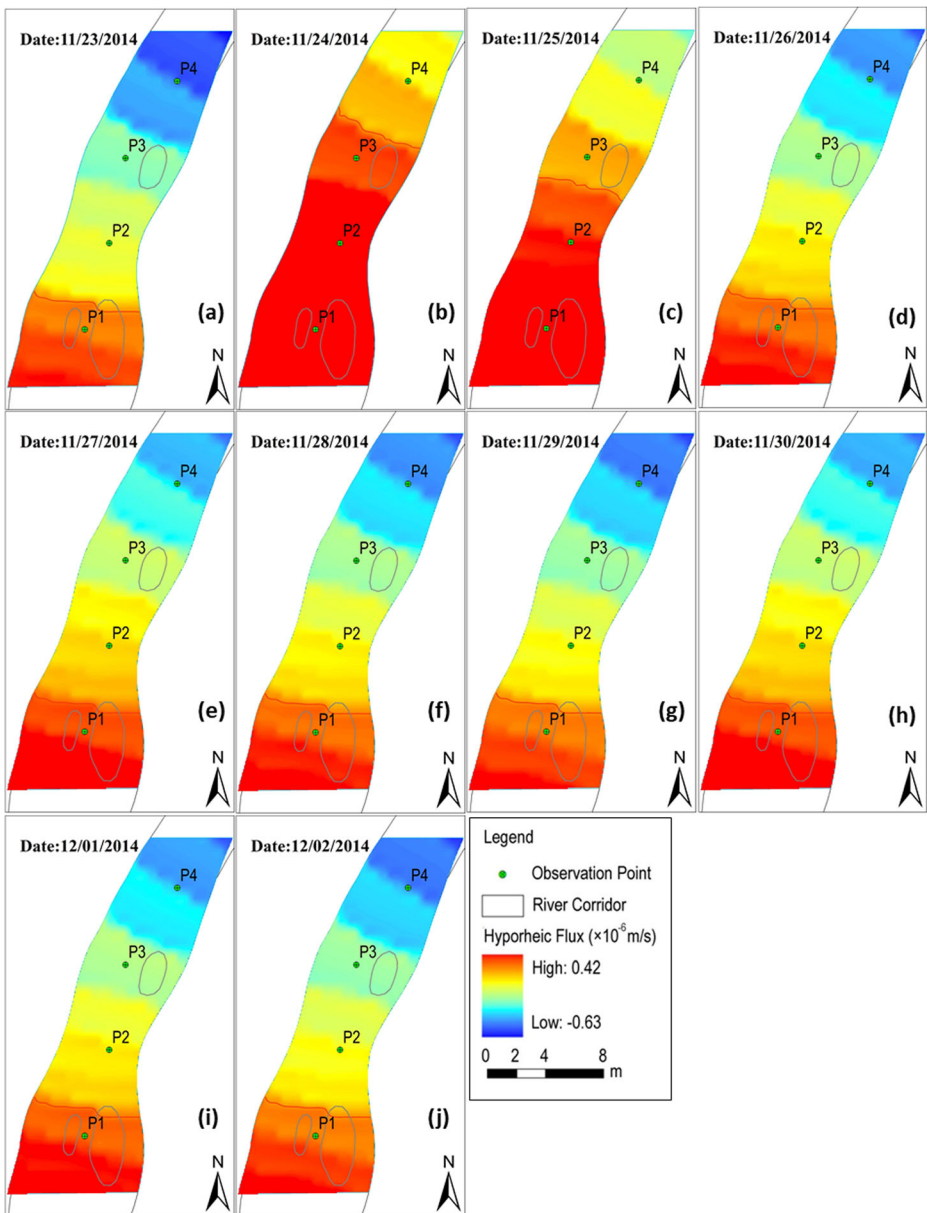
Fig. 3 Transient HEF ($\times 10^{-6}$ m/s) resulting from our numerical simulations. The area with downward flux expanded apparently on 11/24/2014 and 11/25/2014, but the downward flux then degraded gradually after those days. The spatial pattern of flux reverted after the significant rainfall event (on 11/23/2014 ~ 11/25/2014). The red line delineates the boundary between the upward and downward flux zones

vertical hydraulic head gradient evolving over 10 days. Before the first rainfall event, the deeper layer had a larger hydraulic head, and the head for each layer was stable. In each layer, the hydraulic head increased from upstream to downstream. The hydraulic head of the shallower parts of the HZ was driven by the increasing stream stage, resulting in a higher
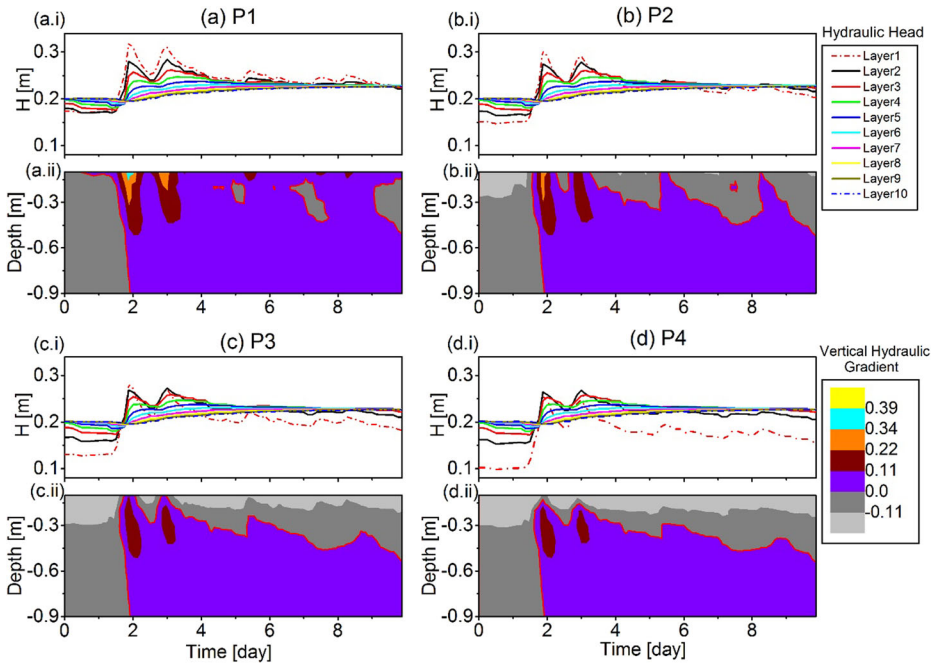
Fig. 4 The modelled hydraulic head (*H*) and the vertical head gradient contour for the selected observation locations P1 (**a**), P2 (**b**), P3 (**c**), and P4 (**d**). The i series shows the hydraulic head, and the ii series shows the head gradient contour. The thick red line shown in the bottom plot of each figure represents the position with a zero head gradient

head than that for the deeper layer (see the i series of Fig. 4). This depth-dependent response to the increasing stream stage caused the reversal of the vertical hydraulic gradient (see the ii series of Fig. 4).

Upstream sections exhibited stronger responses to rainfall than downstream sections. For example, P1, located in the upstream reach, showed an intense response to rainfall. In addition, since deep flow in the HZ was mainly controlled by GW, the hydraulic head of the deep layers increased slightly after the rainfall event. The different response of each layer to rainfall results in different vertical head distributions (see the i series of Fig. 4), and this discrepancy is also (horizontal) location-dependent, as shown by the difference among the curves seen in Figs. 4a.i, b.i, c.i, and d.i. The downstream region had a lower head on the sediment-water interface (SWI) but the same GW upward flux dynamics.

The vertical head gradient in the deep HZ (see the ii series of Fig. 4) exhibited higher variation than that for the shallow HZ. The gradient contour exhibited significant pulses, likely due to rainfall events, but these pulse signals could not reverse all head gradients. As analysed above, the shallow HZ had a more intense response to rainfall, and this also faded faster. Although the deep HZ received a smaller external force than the SWI, the weakened signal took a long time to dissipate. The HZ beneath 0.6 m did not return to its pre-rainfall flow condition during the observation period because the deep HZ required a longer time than the observation period to recover.

Note that the image in Fig. 4d.ii indicates that the shallowest part of the HZ did not show any downward flux or a reversed head gradient during the 10-day test, while the deep HZ showed a reversal of the head gradient. This result reveals that the duration of the reverse head gradient at the shallow HZ decreased downstream and eventually disappeared at S4 (P4).

3.3 Transient Hyporheic Behaviour Driven by Seasonal Hydrological Variation

To investigate the change in hydraulic head in the HZ under the condition of seasonal hydrologic variation, a new coupled numerical model was developed to simulate the HE behaviour lasting for a hydrologic year. The resulting hydraulic head and vertical hydraulic gradient for the four locations are shown in Fig. 5.
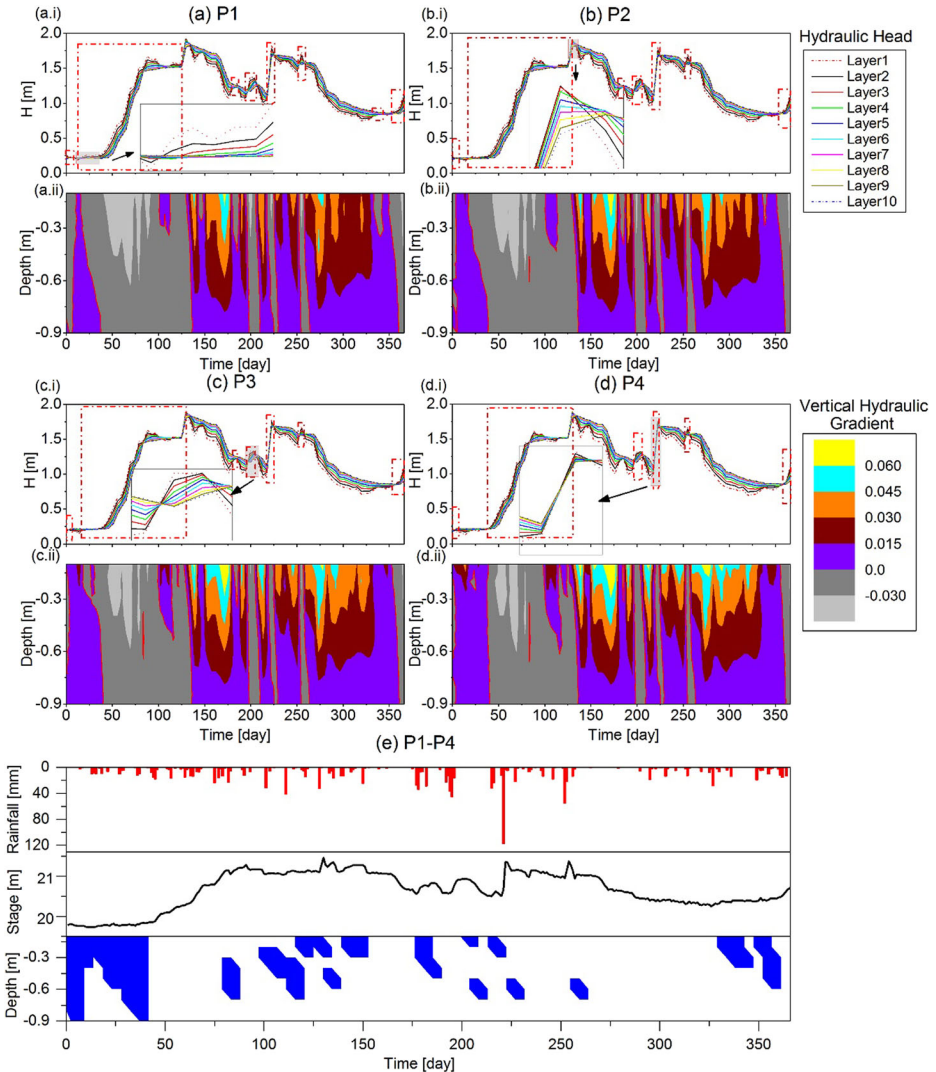
Fig. 5 The modelled hydraulic head (*H*) depicted in the i series and the vertical hydraulic gradient contour shown by the ii series for the selected observation locations P1 (**a**), P2 (**b**), P3 (**c**), and P4 (**d**) for a hydrologic year. These points are located at the middle of the survey river sections. The thick red line shown in the bottom plot of each figure represents the position with a zero hydraulic gradient. (**e**) consists of three small charts, the first two of which are the histogram of annual rainfall and the process of annual water level. The blue part in the third chart shows the difference between the grey areas of P1 and P4 in the ii series. The grey part where the groundwater level reversed of each subplot (from **a**-**d**) has been enlarged and displayed in the figure

Figure 5 provides not only the same information as the single rainfall event but also new findings compared with those of the short duration modelling. The phenomenon of head reversal is observed at each of the four locations, which was the same as the previous model based on a short field observation and a small time step. The reversal of the hydraulic head was closely related to the variation pattern of the hydraulic head. In Fig. 5, there were several increasing periods of the hydraulic head, such as from day 14 to day 97, from day 120 to day 130, etc. The period of increasing GW level always corresponded to the period of river stage as shown in Fig. 5a-d. This result shows that the increase in the river stage caused by a rainfall event can result in the reversal of the hydraulic gradient in the vertical direction. The increase in the groundwater head is only slightly earlier than the reversal of the hydraulic gradient, resulting from the rapid response of the shallow HZ to rainfall. Multiple reversals of the vertical hydraulic gradient were observed. Moreover, the duration and frequency of the hydraulic gradient reversal slightly decreased from upstream (P1) to downstream (P4). The combined effects of rainfall and GW lead to the change in vertical flow direction in the HZ, and the reversals of the hydraulic gradient direction always occurred in the rising phase of the river stage.

It is noteworthy that the hydraulic head for each layer had a slight difference among the four locations (P1, P2, P3, and P4), and hence the vertical hydraulic gradient contours had no apparent significant difference. To determine whether transient HE occurred, the sign of the HF difference between P4 and P1 was calculated and is shown in the bottom plot of Fig. 5e. The blue area in the bottom plot of Fig. 5e indicates the location where the flow direction at P1 is downward while the flow direction at P4 is upward. These areas where transient exchange occurred when the hydraulic gradient started to reverse, but the transient HE did not last long (not until the new hydraulic balance was achieved afterwards, driven by the increased river stage). The occurrence of transient HE also varied with depth. In some areas, the upper HZ did not exhibit transient HE, while the deeper HZ had some short-duration transient HE. This process was caused by the duration of the river stage increase being relatively short. In this case, the signal of the increasing hydraulic head could propagate deep and downward, but the original signal was attenuated by the subsequent river stage and the surrounding hydraulic forces.

4 Discussion

4.1 Conceptual Model for the Transient Dynamics of Hyporheic Flow

We observed the temporal hyporheic flow related to rainfall for a gaining stream. This result was consistent with the findings by Dudley-Southern and Binley (2015), who provided evidence that storm events could be a key driver of the enhanced HE in gaining river systems. A modified conceptual model, which originated from the model proposed by Dudley-Southern and Binley (2015), was applied here to further interpret the transient HE (Fig. 6). The stream could generally gain water from GW (Fig. 6a). Our field investigation and analyses showed that temporal HE occurred while the stream stage increased due to rainfall (Fig. 6b). Because the regional GW head was still significantly higher than the stream stage, upwelling flux dominated the HZ (Fig. 6c) after the influence of rainfall.

Dudley-Southern and Binley (2015) proposed a conceptual model to depict the interaction between SW and GW along a transverse section of a channel using time-dependent electrical
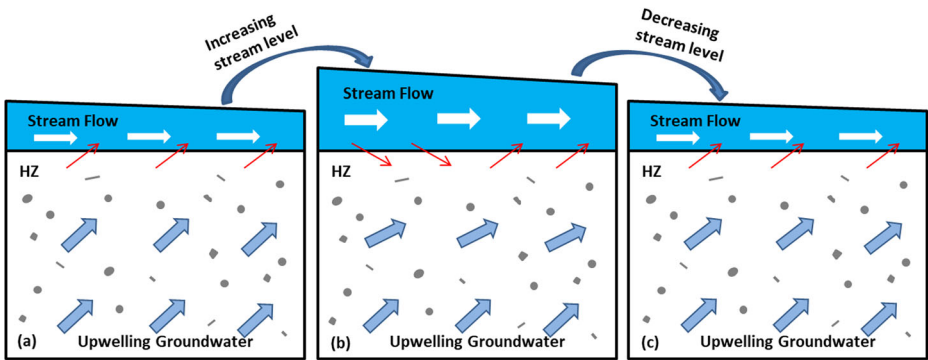
Fig. 6 Conceptual model depicting transient HE driven by a rainfall event. Before the rainfall event, the upwelling GW drives the gaining status (shown by the thin red arrow) at the SWI (**a**). With the water stage quickly increasing by rainfall, the pressure of the upper stream is greater than the head of the shallow HZ, resulting in lost flow (**b**). However, this deduced reverse vertical gradient does not appear downstream because of the lower stream water level and the insufficient head difference between the stream and GW downstream. Therefore, the HE is formed at the shallow HZ. After the rainfall event, the vertical gradient will return to that before the event (**c**)

conductivity profiles, where the reversed vertical hydraulic gradient could be explained using the rainfall event. In addition, two main physical processes were found to control HE during the period of the fluctuating stream stage by Zimmer and Lautz (2014). The first process was the increase in the hydraulic head at the SWI as the stream stage increased, and the second process was the increase in the hydraulic gradient towards the stream resulting from storm water recharge to the adjacent aquifer, which decreased the size of the HZ.

The extended conceptual model based on Dudley-Southern and Binley (2015) mentioned above shows that the HE along the streamflow direction can be generated by subsequent river-stage changes due to rainfall, even if there is no HE observed before the event. This conceptual hyporheic flow model combined with the original model of Dudley-Southern and Binley (2015) provides an additional mechanism to the commonly reported hydraulic "pumping" and "turnover" induced by moving bedforms in the case of submerged bedforms (Elliott and Brooks 1997) or hyporheic flows dominated by quasi-steady hydrostatic pressure gradients across non-submerged instream features such as sand or gravel bars (Trauth et al. 2015). The significance of this hyporheic flow lies in its temporality.

4.2 Factors Affecting the Temporal HE

Two factors that may affect the transient hyporheic flow, including the anisotropic ratio of the hydraulic conductivity and the GW flux, were explored using numerical simulation. Our model calibration revealed that the major factor controlling the temporal HE was the anisotropic ratio of the hydraulic conductivity of the riverbed sediments. Hester et al. (2013) concluded that the anisotropy of K had little effect on the mixing of SW/GW in a homogenous riverbed compared with the impact of the variations in both the hydraulic conductivity (K) and the lower boundary GW flux rate on SW/GW mixing. However, for a heterogeneous case, the interaction between SW and GW would be more closely related to the anisotropy of K. In Hester et al. (2013), the value of anisotropy ranged from 1:1 to 10:1, which originated from many tests and simulations for a single aquifer. For the HZ, which is the shallow part of a riverbed, the exact anisotropic ratio of K contains high uncertainty. A wider range of

anisotropic ratios may exist for an HZ exhibiting clogging. Naranjo et al. (2013) found that streambed layering and anisotropy beneath riffle-pool sequences reduced the overall permeability and the depth of HE and thus increased the mean residence times of water relative to the homogenous isotropic condition.

Three scenarios were selected to test the impact of the anisotropy of hydraulic conductivity on HE: an isotropic high K, an isotropic low K, and an anisotropic K. For the first scenario with a high K, medium transmissivity was much larger than that in the other scenarios, resulting in an almost identical hydraulic head in all layers. No vertical gradient was observed during the rainfall event for this scenario. For the second scenario with a low K (because of the isotropy of K) the hydraulic heads at different layers exhibited minor differences, while the head distribution for all layers differed significantly from the steady state because of the small transmissivity of the streambed. For this scenario, the hydraulic head field needed a longer time to revert to the steady state, and no reversal in the hydraulic gradient could be modelled.

The anisotropic K assumed by the third scenario was the necessary condition to produce the temporal HE patterns discussed above, without the detailed mapping of a medium's fine-scale heterogeneity. Real-world streambed sediment usually has an anisotropic K, for example, due to sedimentary/biological clogging (Boano et al. 2014). As mentioned above, the clogging layer consisting of fine particles resulted in the systematically anisotropic characteristic of HZ. A previous study showed that the hydraulic conductivity ratio of gravel to clay may range from 10^{-3} to 10^{-6} (Todd 1980). The anisotropic ratio of K on the order of 10^{-4} calibrated by our model (which produced the HE closest to that discussed above) indicated that the vertical flow was much slower than the horizontal flow. The forces coming from the stream stage need to propagate for a while before reaching the deep layers of the HZ. Similarly, the upward flow of GW could not immediately affect the shallow HZ. It is the hysteretic hydraulic transmission between SW and GW flow in the HZ (as shown, for example, by Fig. 1c) that generates the temporal HE.

The other factor that may affect the exchange process is upward GW flux. Briggs et al. (2014) indicated that the upwelling flow brought more uncertainty to the estimated HE by using the heat tracing method. The low permeable medium would change the HE pattern under different upward GW fluxes (Gomez-Velez et al. 2014; Lu et al. 2018; Su et al. 2018). This study is the first to quantitatively evaluate the HE affected by both the anisotropic hydraulic conductivity of riverbed sediments and the upward GW flux. Note that the upward GW flux did not directly generate temporal HE but affected the extent and duration of HE. To compare with the results shown in Section 3.2, we tested various GW fluxes. For a larger upward GW flux, the temporal HE could be observed only at the shallower part of the HZ and in the upstream section of the channel. This is because the upward GW movement hinders the downward hyporheic flow. Moreover, a smaller upward GW flux enhanced the vertical and horizontal extents of the temporal HE, and the initial flow field needed more time to recover. In summary, upward GW reduces the possibility of temporal HE driven by rainfall events; see also the work by Trauth et al. (2013). This result may have profound meanings for biochemical processes affected significantly by SW/GW mixing.

4.3 Limitations of this Study

The methods of manual flow measurement in the field and numerical simulation have limitations and can introduce uncertainty. The basic motivation comes from the field investigation of flow measurements before and after the three rainfall events. We observed a

significant overturn of HF in the three stream segments. However, measurement errors still exist within our flow measurements. Manually, flow measurements at four different cross-sections should be inevitable, with some errors due to the asynchrony and spatial discretization of flow measurements. Therefore, the field investigation provides only the change pattern of HF, and the temporal HE is analysed through the numerical simulation. We admit that the accurate field measurements are vital to the deep understanding of temporal HE, and further field studies will be needed to avoid the errors generated by manual operation.

The method of numerical simulation also introduces uncertainty to the analyses of HE. The 1D thermal-based method can provide only the vertical HEF, and the horizontal HEF is still unknown. In other words, the 2D HE images are flexible. That is why the coupled numerical model was used to validate the conceptual model extracted from the 1D thermal analyses. A two-step numerical simulation is generally applied to reproduce the HF field. The feedback of MODFLOW to MIKE 21 was not included in our simulation, although this approach would be applicable for the case of small hyporheic flux compared with streamflow. The hyporheic flow estimated from the thermal method is generally less than 0.026% of the measured streamflow. Therefore, the possible uncertainty of the simulation is insignificant since the two-step simulation is not a fully coupled model in this study. However, the introduced error may be nonnegligible for an HZ with a more positive HE.

5 Conclusions

A ten-day field investigation was performed to explore the potential dynamics in reach-scale SW-GW interactions in the Zhongtian River, China. Detailed observations of the stream corridor, approximately 30 m long and 10 m wide, identified the topography on the scale of the stream corridor. The results of in-situ permeameter tests showed that the permeability of streambed sediment exhibited a certain spatial variability. Field data analysis and model evaluation of the HE led to the following main conclusions.

First, the observed temperature profiles and numerical simulation showed that there was a local flow pattern evolving with time. Driven by several rainfall events, the river stage increased, and the GW level increased but with a delay of $1 \sim 2$ days. The resultant upward GW flow maintained the gaining condition for 10 days. It was interesting to observe the downward flow in part of the reach, which indicated that in this part, the effect of SW pressure on the flux direction was overshadowing the deep HF. Our simulation showed that the reason was likely due to the response time of the stream stage to rainfall being faster than that of GW (due to the anisotropic HZ hydraulic conductivity), resulting in an "abnormal gradient" mapped on the local HF system. This scenario can cause complex, transient local flow patterns, whose confirmation and prediction require a detailed and coupled SW-GW flow model. This model would require a much finer survey of the study site and will be the focus of a future study.

Second, an updated conceptual model was proposed to interpret transient HF, and sensitivity analysis showed that the hydraulic conductivity of the streambed and the upward GW flux may have different impacts on the temporal HE. The transient HF can be well explained by this conceptual model, and the general patterns of HEF agreed with those obtained through numerical simulations. Through 3D numerical modelling, the occurrence of temporal HE was simulated, as was the process of pressure dissipation with depth. Two factors, the anisotropy of hydraulic conductivity and the GW flux, were then discussed to evaluate their impacts on the temporal HE. An isotropic K field could not produce the temporal hyporheic flux. The

hindering effect of upward GW on the extent and duration of the temporal HE was also verified using the anisotropic HZ. The general conclusion that GW flow significantly affects HE patterns and dynamics is in line with the results of some previous studies (e.g., Cardenas and Wilson 2007; Trauth et al. 2013, 2015) .

Third, both the reversed hydraulic gradient and the transient HE were observed through the numerical simulations. The case studies with two different time scales, including a single rainfall event and a hydrologic year, revealed that hydraulic gradient reversal appeared consecutively and could last for a long time, while the stream stage rose due to rainfall. However, transient HE exists in some sporadic time zones and is dependent on the depth. This complex physical phenomenon is also dominated by the stream stage variation driven by rainfall.

The spatiotemporal pattern of HEF may have profound meanings for the river dynamics. The transient nature of HE was highlighted by the proposed and validated conceptual model, revealing its fragility and diversity. The results of this study, therefore, shed light on future investigations of transient HE dynamics.

Compliance with Ethical Standards

Conflict of Interest   The authors declare that they have no conflict of interest.

References

Boano F, Harvey JW, Marion A, Packman AI, Revelli R, Ridolfi L, Wörman A (2014) Hyporheic flow and transport processes: mechanisms, models, and biogeochemical implications. Rev Geophys 52:603–679. https://doi.org/10.1002/2012RG000417

Briggs MA, Lautz LK, Buckley SF, Lane JW (2014) Practical limitations on the use of diurnal temperature signals to quantify groundwater upwelling. J Hydrol 519:1739–1751. https://doi.org/10.1016/j.jhydrol.2014.09.030

Buffington JM, Tonina D (2009) Hyporheic exchange in mountain rivers II: effects of channel morphology on mechanics, scales, and rates of exchange. Geogr Compass 3:1038–1062. https://doi.org/10.1111/j.1749-8198.2009.00225.x

Cardenas MB, Wilson JL (2007) Exchange across a sediment-water interface with ambient groundwater discharge. J Hydrol 346:69–80

Casas-Mulet R, Alfredsen K, Hamududu B, Timalsina NP (2015) The effects of hydropeaking on hyporheic interactions based on field experiments. Hydrol Process 29:1370–1384. https://doi.org/10.1002/hyp.10264

Dudley-Southern M, Binley A (2015) Temporal responses of groundwater-surface water exchange to successive storm events. Water Resour Res 51:1112–1126. https://doi.org/10.1002/2014wr016623

Elliott AH, Brooks NH (1997) Transfer of nonsorbing solutes to a streambed with bed forms: theory. Water Resour Res 33:123–136. https://doi.org/10.1029/96WR02784

Endreny T, Lautz L, Siegel D (2011a) Hyporheic flow path response to hydraulic jumps at river steps: Hydrostatic model simulations. Water Resour Res 47:W02518. https://doi.org/10.1029/2010wr010014

Endreny T, Lautz L, Siegel DI (2011b) Hyporheic flow path response to hydraulic jumps at river steps: Flume and hydrodynamic models. Water Resour Res 47:W02517. https://doi.org/10.1029/2009wr008631

Gerecht KE, Cardenas MB, Guswa AJ, Sawyer AH, Nowinski JD, Swanson TE (2011) Dynamics of hyporheic flow and heat transport across a bed-to-bank continuum in a large regulated river. Water Resour Res 47: W03524. https://doi.org/10.1029/2010wr009794

Gomez-Velez JD, Krause S, Wilson JL (2014) Effect of low-permeability layers on spatial patterns of hyporheic exchange and groundwater upwelling. Water Resour Res 50:5196–5215. https://doi.org/10.1002/2013wr015054

Han B, Endreny TA (2014) Detailed river stage mapping and head gradient analysis during meander cutoff in a laboratory river. Water Resour Res 50:1689–1703. https://doi.org/10.1002/2013wr013580

Harbaugh AW (2005) MODFLOW-2005, the U.S. Geological Survey modular ground-water model – the Ground-Water Flow Process

Hester ET, Doyle MW (2008) In-stream geomorphic structures as drivers of hyporheic exchange. Water Resour Res 44:W03417. https://doi.org/10.1029/2006wr005810

Hester ET, Young KI, Widdowson MA (2013) Mixing of surface and groundwater induced by riverbed dunes: implications for hyporheic zone definitions and pollutant reactions. Water Resour Res 49:5221–5237. https://doi.org/10.1002/wrcr.20399

Lu C, Yao C, Su X, Jiang Y, Yuan F, Wang M (2018) The influences of a clay lens on the hyporheic exchange in a sand dune. Water 10:826

Naranjo RC, Pohll G, Niswonger RG, Stone M, Mckay A (2013) Using heat as a tracer to estimate spatially distributed mean residence times in the hyporheic zone of a riffle-pool sequence. Water Resour Res 49:3697–3711. https://doi.org/10.1002/wrcr.20306

Sawyer AH, Cardenas MB (2012) Effect of experimental wood addition on hyporheic exchange and thermal dynamics in a losing meadow stream. Water Resour Res 48:W10537. https://doi.org/10.1029/2011wr011776

Siergieiev D, Ehlert L, Reimann T, Lundberg A, Liedl R (2015) Modelling hyporheic processes for regulated rivers under transient hydrological and hydrogeological conditions. Hydrol Earth Syst Sci 19:329–340. https://doi.org/10.5194/hess-19-329-2015

Storey RG, Howard KWF, Williams DD (2003) Factors controlling riffle-scale hyporheic exchange flows and their seasonal changes in a gaining stream: a three-dimensional groundwater flow model. Water Resour Res 39. https://doi.org/10.1029/2002wr001367

Su X, Shu L, Lu C (2018) Impact of a low-permeability lens on dune-induced hyporheic exchange. Hydrol Sci J 63:818–835. https://doi.org/10.1080/02626667.2018.1453611

Todd DK (1980) Groundwater hydrology. Wiley, New York

Trauth N, Schmidt C, Maier U, Vieweg M, Fleckenstein JH (2013) Coupled 3-D stream flow and hyporheic flow model under varying stream and ambient groundwater flow conditions in a pool-riffle system. Water Resour Res 49:5834–5850. https://doi.org/10.1002/wrcr.20442

Trauth N, Schmidt C, Vieweg M, Oswald SE, Fleckenstein JH (2015) Hydraulic controls of in-stream gravel bar hyporheic exchange and reactions. Water Resour Res 51:2243–2263. https://doi.org/10.1002/2014WR015857

Weber MD, Booth EG, Loheide SP (2013) Dynamic ice formation in channels as a driver for stream-aquifer interactions. Geophys Res Lett 40:3408–3412. https://doi.org/10.1002/grl.50620

Zhou T et al (2018) Riverbed hydrologic exchange dynamics in a large regulated river reach. Water Resour Res 54:2715–2730. https://doi.org/10.1002/2017wr020508

Zimmer MA, Lautz LK (2014) Temporal and spatial response of hyporheic zone geochemistry to a storm event. Hydrol Process 28:2324–2337. https://doi.org/10.1002/hyp.9778

Affiliations

Chengpeng Lu[1] · Keyan Ji[1] · Yong Zhang[2] · Jan H. Fleckenstein[3] · Chunmiao Zheng[4] · Kate Salsky[2]

[1]   College of Hydrology and Water Resources, Hohai University, Nanjing 210098 Jiangsu, China

[2]   Department of Geological Sciences, University of Alabama, Tuscaloosa, AL 35487, USA

[3]   Department of Hydrogeology, Helmholtz Center for Environmental Research, UFZ, Leipzig, Germany

[4]   School of Environmental Science & Engineering, Southern University of Science and Technology, Shenzhen 518055 Guangdong, China